Open Ceramics 14 (2023) 100350

Contents lists available at ScienceDirect

Open Ceramics

journal homepage: www.sciencedirect.com/journal/open-ceramics

Polymer-derived Ni/SiOC materials structured by vat-based photopolymerization with catalytic activity in CO_2 methanation

Johannes Essmeister [a,1], Lisa Schachtner [a,1], Eva Szoldatits [b], Sabine Schwarz [c], Antonia Lichtenegger [d], Bernhard Baumann [d], Karin Föttinger [b], Thomas Konegger [a,*]

[a] TU Wien, Institute of Chemical Technologies and Analytics, Getreidemarkt 9/164-CT, 1060, Vienna, Austria
[b] TU Wien, Institute of Materials Chemistry, Getreidemarkt 9, 1060, Vienna, Austria
[c] TU Wien, University Service Centre for Transmission Electron Microscopy, Wiedner Hauptstrasse 8–10, 1040, Vienna, Austria
[d] Medical University of Vienna, Center for Medical Physics and Biomedical Engineering, Waehringer Guertel 18-20, 1090, Vienna, Austria

ARTICLE INFO

Handling Editor: P Colombo

Keywords:
Polymer-derived ceramics
Metal modification
Stereolithography
Additive manufacturing
Silicon oxycarbide
Catalysis

ABSTRACT

A new concept for the additive manufacturing of nickel-modified polymer-derived ceramics via vat-based photopolymerization is presented. A photoactive polysiloxane resin system modified by nickel nitrate via methacrylic acid complexation was developed and modified to facilitate vat-based photopolymerization. Through pyrolysis of the Ni-modified preceramic polymer at temperatures between 600 and 800 °C, amorphous SiOC components with well-dispersed Ni nanoparticles can be obtained. The modified polymer and the fabricated structures were characterized by photorheology, thermal analysis, scanning and transmission electron microscopy, optical coherence tomography, and powder X-ray diffraction. In addition, the effect of pyrolysis temperature on specific surface area, crystallinity, and shrinkage was investigated. The developed material systems enable additive manufacturing of porous SiOC structures containing crystalline, uniformly distributed, and bimodally sized Ni nanoparticles, exhibiting catalytic activity suitable for CO_2 methanation. The developed printable SiOC/Ni materials represent a promising approach for combining metal-modified polymer-derived ceramic systems and additive manufacturing for prospective catalysis applications.

1. Introduction

Polymer-derived ceramics (PDCs) are an attractive class of materials as they exhibit the high strength and thermal stability typical of ceramics [1]. As PDCs are obtained from polymeric precursors, a wide range of material combinations are available which are not accessible by classic powder-based production routes. In particular, the modification of PDCs by transition metals has been of particular scientific interest in recent years to obtain materials for potential use in magnetic applications, heterogeneous catalysis, or in medical applications [2–7]. Three main synthesis methods have emerged for this purpose: the physical mixing of polymers and metal (oxide) powders, the synthesis of metallopolymers and the derivatization of polymers by metal complexes [8]. The latter method is particularly appealing due to its flexibility and simplicity. Here, the various metals can be introduced into the preceramic polymer either as inorganic compounds such as metal nitrates, chlorides or acetates [9–11], or as organic compounds including metal acetylacetonates, alkoxides, or amino complexes [3,12–16]. Either the metal compounds react directly with the preceramic polymer, which invariably involves cross-linking of the polymer, or complexing compounds are added to ensure bonding of the metal to the polymer backbone [3,5,17]. In this manner, several transition metals can be incorporated into PDCs, first examples including noble metals such as Au, Ag, Pt, and Cu [18–20]. In this case, the metal particles are present in elemental form within the ceramic matrix after pyrolysis. It was further shown that base metals such as Fe, Co, Ni, Ti, Hf, Mo, W, and Zr could also be incorporated [5,10,21–26]. Different phase compositions can be obtained depending on the metal's tendency to form carbides or silicides.

In recent years, increasing scientific interest into using these materials as heterogeneous catalysts has emerged. Here, the intrinsic porosity of PDCs generated during the pyrolysis of the material proves advantageous, as it provides a large active surface area. Various efforts were made to tailor the porosity and surface of the PDCs in combination with

* Corresponding author.
E-mail address: thomas.konegger@tuwien.ac.at (T. Konegger).
[1] These authors contributed equally: Johannes Essmeister, Lisa Schachtner.

https://doi.org/10.1016/j.oceram.2023.100350
Received 14 December 2022; Received in revised form 16 February 2023; Accepted 23 March 2023
Available online 24 March 2023

metal modification [27]. Together with the particularly favourable temperature stability of PDC materials, it was possible to generate high-performance catalysts for various applications. In the case of catalysts for hydrogen evolution reaction, *Feng* et al. [5] presented the use of Mo in the form of a $Mo_{3+2x}Si_3C_{0.6}$ phase, and *Yu* et al. [26] generated WC and W_2C within a polycarbosilane-derived matrix as effective catalysts. *Sachau* et al. [14] demonstrated the use of Pt within a SiCN matrix for the hydrolysis of sodium borohydride. In a similar approach, *Glatz* et al. [18] achieved selective hydrocarbon oxidation with the use of Cu within a SiCN ceramic. With regard to the dry reforming of methane, *Wang* et al. [28] used Pd as an effective catalyst within a SiOCN matrix. Furthermore, *Yu* et al. [29] demonstrated the catalytic ability of Fe_3O_4/SiOC composites in the degradation of xylenol orange. In this context, it is vital to highlight Ni, which has been studied intensively in the context of heterogeneous catalysis. *Zaheer* et al. [6], for instance, incorporated Ni into a polymer-derived SiC matrix and tested the catalyst's suitability for the hydrolysis of benzyl phenyl ether. With regard to polycarbosilane-derived materials, *Kaur* et al. [4] were able to show that suitable catalysts for CO_2 methanation can be produced by introducing Ni into a PDC matrix. Similarly, *Macedo* et al. [10] were able to show that the introduction of Ni into polysiloxanes provides robust catalysts for use in CO_2 methanation. However, all approaches mentioned so far are limited in terms of shapeability, the resulting materials being obtained exclusively as powders. As powder-based catalysts exhibit considerable disadvantages in technical applications, including back-pressure build-up within the reactor or complications during reactor filling, the next step in successfully implementing these materials requires a distinct focus on the shaping of metal-modified PDCs. In this context, *Schumacher* et al. [3] reported on an approach to produce a PDC-based monolithic catalyst via freeze-casting and modification with Ni. However, as the determination of the catalytic activity was also only carried out in powdered form, a clear evaluation of the suitability of monolithic PDC-based components as catalysts remains missing.

Additive manufacturing (AM) has become an attractive way of generating complex monolithic components from PDCs in the recent past, which in turn would be ideal for use in heterogeneous catalysis. Different approaches have been developed in the context of PDC-based AM, particularly concerning vat-based photopolymerization (also known as stereolithography) [30–32]. This approach of structuring PDCs has been successfully combined with metal-modified preceramic polymers: for instance, *Fu* et al. [17] were able to show that Ti and Zr can be incorporated into a polysiloxane matrix by using methacrylic acid as a complexing agent. *Ma* et al. [33] demonstrated the introduction of Cu, Co, and Ni into polysiloxanes via a straightforward approach using metal nitrates. Very recently, *Yao* et al. [34] and *Zhou* et al. [35] developed Ti-, Fe-, Co-, and Cu-modified polysiloxanes as base materials for microwave absorbers and sensing structures. However, the prospective use of stereolithography-compatible metal-modified preceramic polymers toward catalysis applications has not yet been addressed.

In this work, Ni-modified polysiloxane-derived ceramics shapeable via stereolithography and applicable for heterogeneous catalysis are reported for the first time. We introduce a new methodology for incorporating Ni into a photosensitive printing resin, and report on the effects of pyrolysis conditions on the resulting phase composition, morphology, and pore evolution. The developed materials exhibit catalytic activity with regard to CO_2 methanation, which we consider highly relevant in the context of current strategies toward mitigation of climate change.

2. Experimental

The development of a photocurable matrix polymer was based on a materials system first reported by Zanchetta et al. [30], consisting of methyl-silsesquioxane and 3-(trimethoxysilyl)-propyl methacrylate (TMSPM) as a cross-linker, and which we recently adapted in our group for the development of additively manufactured SiOC/SiC composites [32].

In a typical experiment, 40 g of methyl-silsesquioxane powder (MK, Silres MK, Wacker-Chemie) were dissolved in 20 g of tri (propyleneglycol)-methyl ether (TPM, Formlabs) and stirred at 150 rpm in a water bath at 70 °C. When fully dissolved, 10 g of TMSPM (98%, Sigma Aldrich) were added as a cross-linker and stirred at room temperature for 1 h. Subsequently, 0.2 g of aqueous hydrochloric acid (HCl, 37%, Sigma-Aldrich) was mixed with 0.8 g of TPM and then slowly added into the flask with constant stirring. The mixture was hydrolysed at room temperature for 20 h under constant stirring. The resulting volatile substances were then evaporated by a rotary evaporator at 45 °C and 100 mbar for 2 h. Finally, 2% Genorad*16 (G*16, RAHN) were added as a stabilising agent, and the resin was thoroughly homogenized using a planetary mixer (Thinky ARE-250; 4 min at 2000 rpm), followed by a degassing step, resulting in the polysiloxane base system (PSO-TMSPM).

To prepare the Ni-modified resin, nickel (II) nitrate hexahydrate (NiN, 99%, Merck) was first dissolved in tetrahydrofuran (THF, ≥99,9%, Riedel-de Haen). The amount of NiN was calculated to correspond to the desired amount of Ni in the final pyrolysed structure, resulting in final Ni contents of 5 wt%. When fully dissolved, methacrylic acid (MAA, 99%, Thermo Scientific) was added as a complexing agent in a Ni/MAA molar ratio of 1:2. The amount of THF added was at minimum three times the amount of MAA, in order to ensure complete dissolution. The solution consisting of NiN, THF, and MAA was then stirred for 1 h at room temperature. To ensure that the two emerging phases do not fully separate, but are instead present as evenly distributed spherical micelles, polyoxyethylene (20) sorbitan monolaurate (Tween 20, Aldrich) as surfactant to promote micelle formation was added before stirring for another 30 min. The amount of Tween 20 corresponded to 5% of trimethylolpropane-trimethacrylate (TMPTMA, technical grade, Sigma-Aldrich), a reactive diluent which was added at a later time. The base preceramic polymer (PSO-TMSPM) was combined with the NiN/THF/MAA solution under stirring. Once all components were combined, the resin was stirred overnight at room temperature.

Before the AM process, the desired amount of TMPTMA was added as a reactive diluent, and the mixture was stirred for 20 min. The TMPTMA content was varied between 10 wt% and 20 wt%. The added amount of hydroquinone (99%, Merck) as additional stabilising agent was 10 mg per mole of double bonds in the final formulation. The flask was then placed in the rotary evaporator for 1 h at 40 °C and 60 mbar to evaporate volatile species and residual THF, which may interfere with the printing process.

Before printing, 1% phenylbis (2,4,6-trimethylbenzoyl) phosphine oxice (BAPO, Genocure*BAPO, 97%, RAHN) was added as a photoinitiator under the exclusion of blue light. The initiator was completely dissolved and mixed into the resin using a planetary mixer. The Ni-free reference sample was prepared using the same procedure, in the absence of nickel (II) nitrate hexahydrate.

2.1. Additive manufacturing

A 3D desktop printer (Elegoo Mars 2 Pro) was used for vat-based photopolymerization. The light exposure was realized with a 2 K monochrome LCD screen with LEDs at a wavelength of 405 nm and an

Table 1
Printing parameters used during printing of PDC-based lattice structures (see Fig. S1 in Supporting Information).

Exposure intensity (mW cm^{-2})	14
Bottom layer count	5
Bottom exposure time (s)	60
Exposure time (s)	18
Layer height (μm)	25

intensity of 14 mW/cm^2. The modified resin tank was equipped with an FEP foil (ELEGOO, FEP 2.0 Release Film Liner, 0.127 mm thickness). The defoamed resin was poured into the tank, and the light cover was placed on top before the printing started. Table 1 shows an example of the selected printing parameters. The exposure time was adjusted based on the individual resin characteristics.

After the printing process, the cured structures were gently detached from the printing platform using a razor blade. The components were then ultrasonically cleaned in TPM for 10 min. Subsequently, the supports were separated from the lattice structure, and compressed air was used to remove any residual uncured resin. The cleaned structures were then carefully dried and stored in a desiccator until pyrolysis was carried out.

2.2. Pyrolytic conversion

The pyrolysis was conducted in a 3-zone split tube furnace (HZS 12/600, Carbolite Gero) under flowing Ar atmosphere (0.6 L/min). The structures were pyrolysed at maximum temperatures ranging from 600 °C to 800 °C for 2 h. The temperature profile consisted of a heating step to 200 °C (0.5 °C/min, 2 h dwell time), a subsequent heating step to 500 °C (1 °C/min, 1 h dwell time), and a final heating step to the maximum temperature (1 °C/min, 2 h dwell time). Cooling to room temperature was carried out at a rate of 2 K/min.

2.3. Characterization

Photopolymerization was investigated using a real-time IR-photorheology setup, as described by *Gorsche* et al. [36], to obtain information on rheological properties and on time-resolved double bond conversion. The setup consisted of a Bruker Vertex 80 FTIR spectrometer equipped with a near-infrared (NIR) optic, coupled with a rapid scan module and an Anton Paar MCR302 WESP rheometer. The measurement parameters were selected to simulate the conditions during AM. A broadband Exfo OmniCure 2000 UV-light source, emitting between 270 nm and 550 nm with an intensity of 15.4 mW, was chosen in combination with an external MCT IR detector (Bruker DigiTect). The rheometer was equipped with a parallel plate steel measurement system with a diameter of 25 mm. The sample thickness was set to a gap of 0.05 mm between the plate and the optical window. All measurements were carried out at room temperature. Before irradiation, the respective resin samples were sheared with a strain of 1% and a constant shear rate of 1 Hz. To adjust the exposure time for the printer, the curing depth was determined at varying exposure times on the DLP desktop printer using a sliding gauge. Thermogravimetric analysis (TGA) and differential thermal analysis (DTA) were conducted using a NETZSCH STA 449 C instrument. A heating ramp of 5 K/min from 30 °C to 1500 °C under flowing Ar atmosphere (50 mL/min) was selected for all measurements, the sample amount consisting of 30–40 mg. In addition, ceramic yield and the linear shrinkage were determined with an analytical balance and a sliding gauge, respectively. Powder X-ray diffraction (XRD) was performed with a PANalytical XPert Pro MPD using Cu$K_{\alpha 1,2}$-radiation at a diffraction angle 2Θ between 5° and 100°. Morphology and macrostructure of printed and pyrolysed structures were observed with a digital microscope (VHX-5000, KEYENCE). Scanning electron microscopy (SEM) images of surfaces and fracture surfaces were recorded using a FEI ESEM Quanta 200 instrument. Complementary to SEM investigations, the printed specimens were imaged using a custom-build visible-light optical coherence tomography (OCT) setup [37]. OCT is a light interferometric imaging technique, which enables three-dimensional, non-destructive examinations of semi-transparent samples in real-time [38]. By utilizing a broadband supercontinuum source (NKT Photonics, SuperK EXTREME EXU-6) in the visible wavelength region, an axial resolution of 1.2 μm in air was achieved in the utilized OCT setup. In addition, a 20x magnification objective lens (UPLFLN 20XP, Olympus) enabled a 2.0 μm lateral image resolution and a field-of-view of 300 x 300 μm^2. OCT volumes were acquired in 8.3 s. After data post-processing, grey-scale images were retrieved, in which regions of low scattering appear dark and regions of highly-scattering particles light grey to white [37]. Transmission electron microscopy (TEM) measurements were recorded using a TECNAI F20 with a field emission gun as an electron source at 200 kV. Scanning transmission electron microscope (STEM) images were recorded using a Gatan DigiSTEM II detector. High resolution-TEM images were recorded using a Gatan Rio 16 camera. For recording the selected area electron diffraction (SAED) patterns, a setup with a wider aperture was chosen (TECNAI G20 with a LaB_6 emitter). Specific surface areas of the materials were determined by N_2 adsorption at −196 °C according to BET theory using 5 measurement points (ASAP 2020, Micromeritics). BJH calculations were used for the determination of pore size in the mesopore range, assuming a cylindrical pore geometry. Depending on the expected specific surface area, between 100 and 200 mg of each sample were weighed in and degassed in vacuum for 4 h at 300 °C prior to measuring.

Testing of the catalytic activitiy during CO_2 methanation was performed in a self-assembled fixed-bed steel reactor with an inner diameter of 6 mm at atmospheric pressure. A mixture of 1 g of catalyst and 1 g of Al_2O_3 as a filler material was first pre-treated at 400 °C for 4 h in 50 ml/min gas flow consisting of 10 vol% H_2 in He. The catalytic activity was evaluated using a feed of 50 ml/min (containing 10 vol% CO_2, 40 vol% H_2 and 50 vol% He) at temperature steps of 50 °C between 200 and 400 °C, with a dwell time of 2 h for each temperature step. The composition of the outlet gases was analysed by gas chromatography using an Inficon Micro GC Fusion instrument.

3. Results and discussion

3.1. Resin characterization

Photorheology coupled with *in-situ* near-infrared (NIR) spectroscopy was carried out to investigate the processes taking place during the photo-initiated curing reaction. Within these investigations, the course of the storage modulus is the most critical rheological factor (Fig. 1 B), which allows conclusions to be drawn about the speed of the reaction and the stiffness of the cured polymer. The second indicator for the processes taking place during the photoreaction is the course of the double bond conversion (DBC), which is derived from the NIR signal during the photoreaction (Fig. 1 A). In addition, the normal force between the two plates can be measured, correlating to the shrinkage of the material during curing (Fig. 1C). The time zero ($t = 0$) indicates the initiation of the reaction by light exposure while oscillating shear stress is maintained. After a steep increase in all measurements, the plateau modulus (G'_{max}) and the final DBC (C_{final}) are reached, and no further reaction can be seen after the initial cure. The starting point of the curing reaction is usually given as the gel point (t_{gel}), characterized by the intersection between the storage modulus (G') and loss modulus (G''). In addition to t_{gel}, the onset of decreasing normal force can be correlated to the initiation of polymerization and its resulting shrinkage within the system. A comparison of both determination variants is given in the Supporting Information (Fig. S2).

The photorheological behaviour of a Ni-free reference resin with 10 wt% TMPTMA and Ni-containing resins with 10 wt%, 15 wt% and 20 wt % TMPTMA were studied. While t_{gel} is lower in the systems doped with Ni than in the reference, it is not affected by the amount of TMPTMA. In addition, t_{gel} is reached at lower double bond conversions (C_{gel}) in the Ni-modified systems. The difference in C_{gel} indicates that gelation of the system takes place at lower conversion rates in Ni-containing systems. In contrast, in the Ni-free reference system, t_{gel} is reached at higher C_{gel} values and at a later time, thus a higher degree of cross-linking is

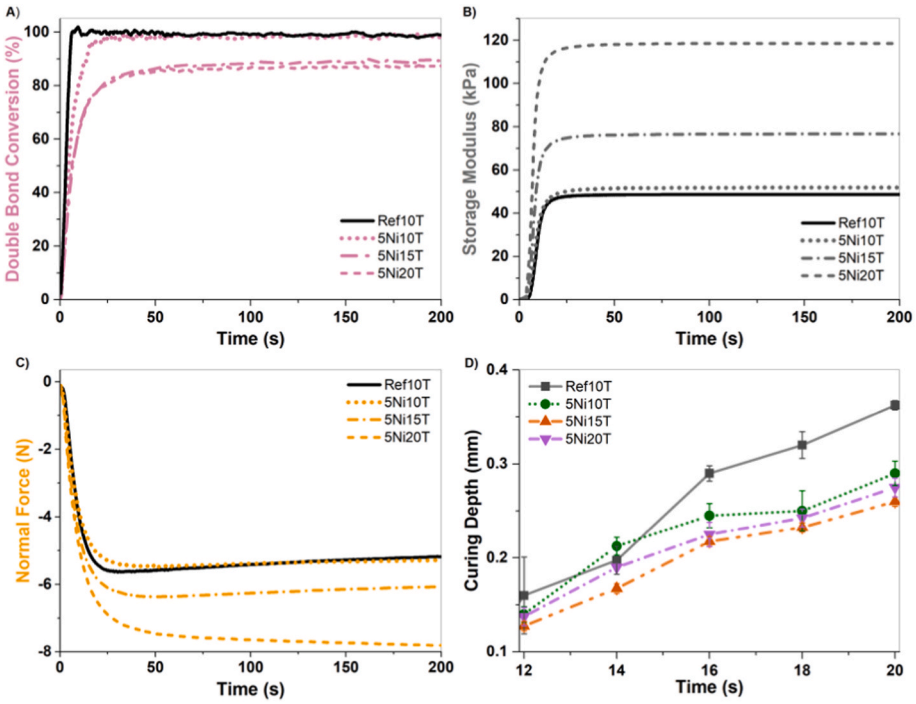

Fig. 1. Curing experiments of reference material with 10 wt% TMPTMA (Ref10T) and Ni-modified systems with 10 wt% (5Ni10T), 15 wt% (5Ni15T), and 20 wt% (5Ni20T) TMPTMA; (A) Double bond conversion calculated from NIR signals; (B) Photorheology - storage modulus; (C) Photorheology - normal force; (D) Curing depth determined by light penetration tests with variation of curing time.

Table 2
NIR-photorheology results including the time to gel point (t_{gel}), double bond conversion at gel point (C_{gel}), final conversion (C_{final}), time to 95% conversion ($t_{95\%}$), maximum storage modulus (G'_{max}), and the normal shrinkage force (F_N) of the reference sample containing 10 wt% TMPTMA (Ref10T) and of Ni-modified systems containing 10 wt% (5Ni10T), 15 wt% (5Ni15T), and 20 wt% (5Ni20T) TMPTMA, respectively.

Resin	t_{gel} (s)	C_{gel} (%)	C_{final} (%)	$t_{95\%}$ (s)	G'_{max} (kPa)	F_N (N)
Ref10T	3.1 ± 0.2	43 ± 9	100 ± 2	5.0 ± 0.3	49 ± 28	−5.1 ± 0.9
5Ni10T	2.3 ± 0.1	18 ± 3	99 ± 1	15 ± 0.5	52 ± 22	−5.2 ± 0.9
5Ni15T	2.3 ± 0.1	17 ± 3	89 ± 7	32 ± 0.3	77 ± 2	−6.0 ± 0.4
5Ni20T	2.2 ± 0.3	14 ± 1	88 ± 3	30 ± 0.6	118 ± 8	−7.9 ± 0.2

required to gel the reference polymer in the absence of Ni (Table 2). In addition, t_{gel} corresponds with the onset of measured normal force, which indicates the polymerization-induced shrinkage and shrinkage stress evolution. The value of the maximum storage modulus (G'_{max}) rises with an increasing amount of TMPTMA, indicating a tighter network to be formed by the additional acrylate. In the case of the Ni-modified systems with a higher TMPTMA content, the increase in stiffness after the start of light exposure is more pronounced. Although higher stiffness values can be achieved at higher TMPTMA contents, there is a decreased slope in double bond conversion, which in turn leads to a longer time required for the completion of the reaction (i.e., a higher $t_{95\%}$). Here, rapid polymerization involving TMPTMA is in competition with kinetic hindrance caused by the phase separation in the system as depicted in Fig. 3. This results in the evolution of a loose network with non-polymerized moieties in between. After prolonged exposure, this material further consolidates through polymerization and pulls the outer lattice together, resulting in more significant shrinkage (F_N), which is a direct consequence of C_{gel} and the conversion after gelation. An increased G' can result in enhanced shrinkage stress (lower F_N value) with respect to conversion toward the final stages of photopolymerization. Ultimately, the Ni-modified systems achieve a lower C_{final} with increasing TMPTMA content. Here, phase separation has a decisive role, since it is more pronounced at increasing TMPTMA content, thus promoting the kinetic hindrance of the photoreaction.

In addition to the photorheological properties of the resins, the cured layer thickness was also investigated (Fig. 1 D). For this purpose, exposure tests were carried out on the 3D printer in order to determine the curing depth as a function of curing time. The reference sample shows a higher curing depth at longer exposure times than the Ni-modified samples. This difference can mainly be attributed to the coloration of the resin due to the nickel nitrate used. Furthermore, the occurrence of the phase separation within the Ni-modified resin causes turbidity, which in turn diminishes the curing depth. As phase separation is more pronounced with rising TMPTMA content, the turbidity of the resin increases. Therefore, the curing depth decreases with increasing TMPTMA content. The effect of nickel nitrate on the curing depth can be seen as an advantage in additive manufacturing, as the Ni-modification also serves as a contrast additive. Thus, a higher resolution of the components can be achieved, and unwanted over-polymerization can be prevented. From the determination of the curing depth and the photorheological data, conclusions can be drawn about the printing properties of the Ni-modified resins depending on the amount of TMPTMA. It can observed that the increase in acrylate content leads to an increase in stiffness, but the final double bond conversion decreases. In addition, increasingly pronounced phase separation can be observed at higher TMPTMA contents, resulting in an upper processing limit of 10 wt% TMPTMA.

Since photorheology was carried out under conditions comparable to those in actual printing, curing depth and $t_{95\%}$ can be directly compared: at the selected printing time of 18 s (Table 1), the polymerization

reaction is largely complete, and a sufficient layer thickness can be produced.

3.2. Morphology and microstructure of printed parts

Highly complex components could successfully be produced with both the Ni-free reference material and the Ni-modified polysiloxane systems, as shown by the lattice structures in Fig. 2. Here, the changing coloration from colorless to green is visible due to the introduction of Ni. Furthermore, the difference between the transparent unmodified material and the opaque modified material becomes apparent. This difference in opacity is a direct consequence of the effect of Ni on phase separation within the polymer system. When handling the components, the Ni-modified variant proved to be more mechanically stable, and components with higher structural integrity could be produced. In case of both materials, minimal strut sizes of 400 μm could be printed, demonstrating the mechanical stability and handleability of the polymerized material. However, higher resolutions are in principle achievable, especially when using the Ni-modified system.

The phase separation occurring due to the different solubility of Ni precursors in the resin components was further investigated using optical coherence tomography (OCT), using printed components. This non-destructive technique makes it possible to identify material heterogeneities within the printed components based on differences in refractive indices, which in turn can be correlated to the phase separation within the material. Fig. 3 A shows a cross-section of a printed, Ni-containing specimen reconstructed from OCT with a penetration depth of several micrometres. The contrast illustrates the heterogeneity within the sample, which is caused by phase separation of Ni-containing constituents, being present as micelles within the component. In Fig. 3 B, showing an en-face image of the same material, two distinctly reflective areas can be identified, again a direct consequence of the presence of

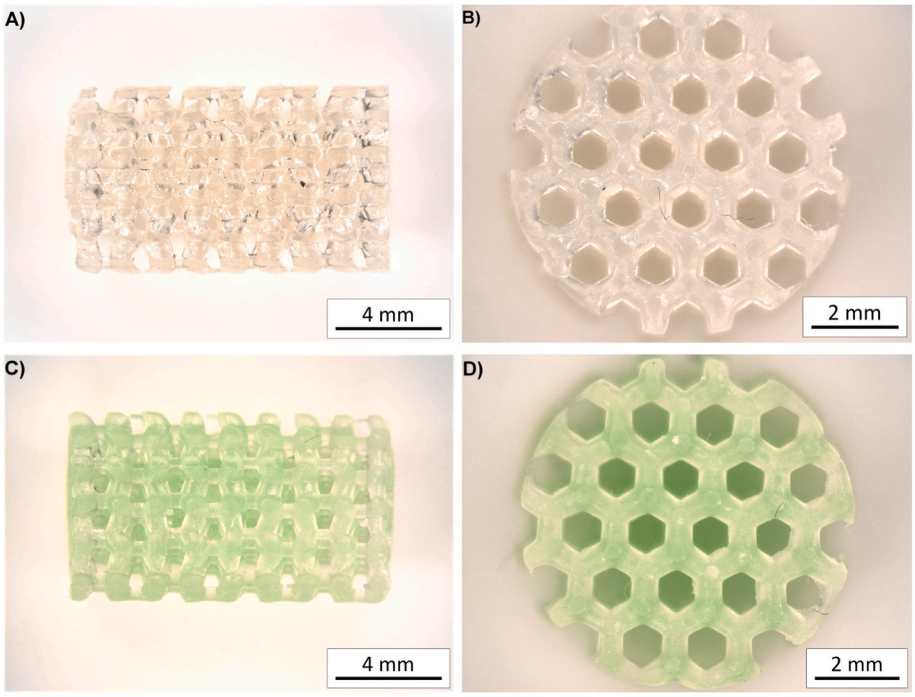

Fig. 2. Printed lattice structures of Ni-free reference specimens and Ni-modified specimens at different magnifications, (A,B) reference material (Ref10T), (C,D) Ni-modified material (5Ni10T).

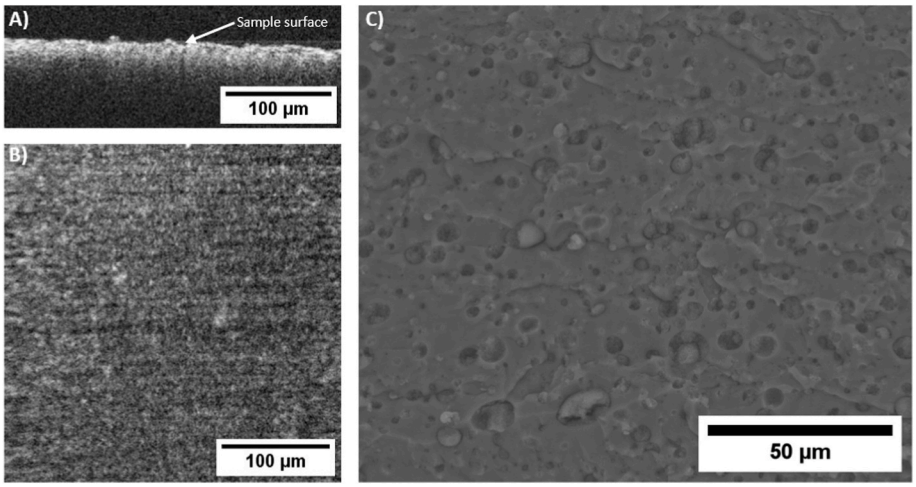

Fig. 3. A) Optical coherence tomography images of printed Ni-modified samples cross-section of Ni-modified sample (5Ni10T), (B) en-face image Ni-modified sample (5Ni10T), C) Backscattered electron image of cross-section of Ni-modified sample (printed part post cured at 130 °C).

micelles in the resin. Additionally, the printing layers are evident as horizontally aligned structures. When comparing the OCT images with a BSE image of a fracture surface from the printed sample post-cured at 130 °C, the micelles are likewise revealed. By combination of these investigation techniques, the presence of micelles within the printed components can be illustrated, with the micelles subsequently being responsible for forming pores during the polymer-to-ceramic conversion process.

3.3. Polymer-to-ceramic conversion

ATR-FTIR measurements of uncured, cured, and pyrolysed samples were carried out, as depicted in Fig. 4. A distinct difference in the signals between the samples before and after pyrolysis can be observed. The signals of asymmetric CH_3 stretching vibrations and C–H stretching vibrations at 2970 cm^{-1} and 2925 cm^{-1} originating from the residual organic groups can be determined in the spectra of the resin and the cured component. These modes fade with an increase in pyrolysis temperature. Other organic residues, which can be identified via C–H bands (1390-1450 cm^{-1}), also disappear after pyrolysis. In addition, the broad mode between 3120 and 3370 cm^{-1} indicative of water is present in the non-pyrolysed materials due to residual water in solvents and Ni(II)nitrate hexahydrate, with the hexahydrate leading to a higher intensity mode in Ni-modified samples. The pyrolysed samples also show water signals, presumably adsorbed to the different samples to varying degrees during storage. The characteristic water signal is not present in the sample pyrolysed at 600 °C, but appears and increases with increasing pyrolysis temperatures. Residual C–H bonds, still present after pyrolysis at 600 °C, result in a hydrophobic material.

The peak assigned to C═C bonds at 1640 cm^{-1} decreases during the curing of the sample, indicating the polymerization of TMSPM. The peak at 940 cm^{-1}, originating from vinyl groups, also broadens after curing and vanishes after pyrolysis. The C═O stretching vibrations at 1720 cm^{-1}, typical of MAA or esters such as TMSPM and TMPTMA, become wider after photocuring due to the change of mobility of the C═O bonds with gradual terminal double bond polymerization [30]. The peak at 1270 cm^{-1}, indicative of R–CH═CH_2 and/or Si–CH_3, decreases with rising pyrolysis temperatures. The modes between 990 and 1120 cm^{-1} can be assigned to several Si–O–Si and Si–O–C stretching vibrations, including the range of 1120–1170 cm^{-1} (indicative of cage structures) and 1030–1060 cm^{-1} (indicative for an Si–O–Si network). As the pyrolysis temperature increases, these signals become a broad single peak with a shoulder at about 1000 cm^{-1}. With increasing pyrolysis temperature, almost all absorption peaks shift slightly and broaden due to the structural reorganization, leading to an increase in the energy for the vibration of each bond [17].

When investigating the pyrolysis process by TGA (Fig. 5 A), the evaporation of residual water and remaining solvents can be seen at temperatures below 250 °C. As soon as the volatile components have evaporated, the conversion and decomposition of the material commence. After the initial weight loss, polycondensation of polysiloxane and consequent release of reaction products such as ethanol and water takes place (between around 250 °C and 450 °C). An exothermic signal in the DTA curve, at about 160 °C, is present in samples modified with Ni, indicating a reaction only taking place in the presence of Ni, with thermal cross-linking being a potential explanation. Photorheology experiments (Table 2) showed that the sample 5Ni10T has a lower double bond conversion than the Ni-free reference material Ref10T, which has a DBC of 100%, and therefore no further thermal cross-linking occurs in Ni-free samples, as opposed to Ni-containing materials.

At higher temperatures (~450–800 °C), the organic groups decompose by cleavage of Si–C, and C–H bonds, releasing methane, hydrogen, and volatile siloxane compounds in the process. At temperatures above 800 °C, mainly H_2 is released. At about 800 °C, the weight loss levels off, indicating that the polymer-to-ceramic conversion has largely been completed [30]. Both the reference sample and the Ni-modified sample exhibit similar temperature transitions. However, due to the catalytic effect of Ni on the polycondensation reactions and decomposition processes during the conversion, the mass loss curve is shifted towards lower temperatures for the Ni-modified sample. Although a faster degradation occurs during the conversion, the Ni-containing sample has a higher residual mass, mainly due to Ni remaining in the ceramic matrix, leaving a higher number of inorganic constituents in the material. As a result, a higher ceramic yield can be observed. Finally, a

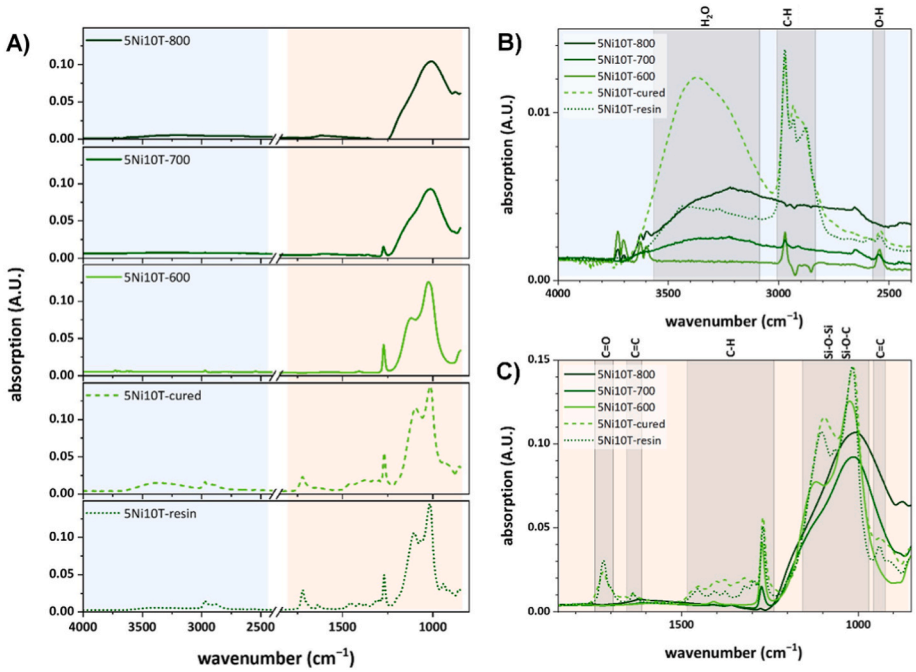

Fig. 4. ATR-FTIR spectra of the 5Ni10T formulation. (A) Individual spectra of the resin, printed component, and the material after pyrolysis in Ar at 600 °C, 700 °C and 800 °C, in the range from 4000 to 850 cm^{-1}. (B) Overlay of all five spectra in the region of 4000-2400 cm^{-1}. (C) Overlay of all five spectra in the region of 1850-850 cm^{-1}.

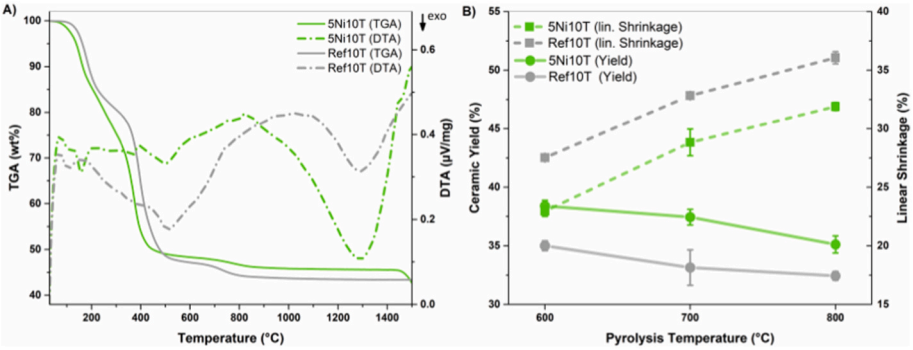

Fig. 5. A) Simultaneous thermal analysis (TGA/DTA) of cross-linked samples in Ar atmosphere, B) Determination of ceramic yield and linear shrinkage (diameter of the 3D printed lattice); 5Ni10T (green) and reference material Ref10T (grey).

degradation of the Ni-modified ceramic material at 1450 °C becomes evident, owing to the carbothermic reduction of the SiO_2 phase, which is shifted to lower temperatures by the presence of the metal [39].

The linear shrinkage and ceramic yield of the lattice samples were determined by determining diameter and mass before and after pyrolysis, respectively (Fig. 5 B). The difference between the Ni-modified sample and the reference sample is evident, as a higher ceramic yield and lower shrinkage are obtained with the introduction of Ni. Consequently, the ceramic yield increases by 4%, while the linear shrinkage decreases by 2.6%, after pyrolysis at 800 °C. Overall, the typical temperature-dependent behaviour of PDCs can be observed, with linear shrinkage increasing and ceramic yield decreasing with increasing pyrolysis temperatures.

3.4. Properties of pyrolysed materials

3.4.1. Macrostructure of additively-manufactured components

The printed lattice structures were successfully converted into ceramic components at 600, 700, and 800 °C. Fig. 6 shows components derived from a Ni-free reference material as well as from the Ni-modified material after pyrolysis at a maximum temperature of 800 °C. Crack formation in the ceramics was observed, caused by shrinkage of the material and outgassing of volatile components. Due to the high content of organic components in the resin formulations, the high shrinkage and the low ceramic yield play a crucial role here. Similar component morphologies were also found at lower pyrolysis temperatures. However, no influence of the Ni modification on the crack formation could be found, as both systems show a similar tendency in this respect. The Ni-modified sample surfaces appear less reflective than in case of the reference sample. The increased surface roughness due to the formation of micelles in the Ni-containing system is responsible for this appearance, as can also be seen in Fig. 7 A. Apart from the formation of cracks, the printed structures could be produced without distortion or anisotropic shrinkage. Although the cracks present are not beneficial from a mechanical point of view, they can still be seen as channels for additional gas exchange, which in turn can be beneficial in catalysis [40,41].

3.4.2. Microstructure and phase composition

The morphology of the surface and internal structure of the printed specimens was investigated by SEM. For Ni-modified samples pyrolysed at 800 °C, a rough surface was found, composed of closed macropores. These pores, remnants of the micelles within the printing resin, can be seen in Fig. 7 A. Again, similar structures were found at all three pyrolysis temperatures investigated. In Fig. 7 B, a cross-section at the edge of the sample is shown. The most noticeable aspect here is a dense layer close to the component's surface, extending approximately 60 µm into

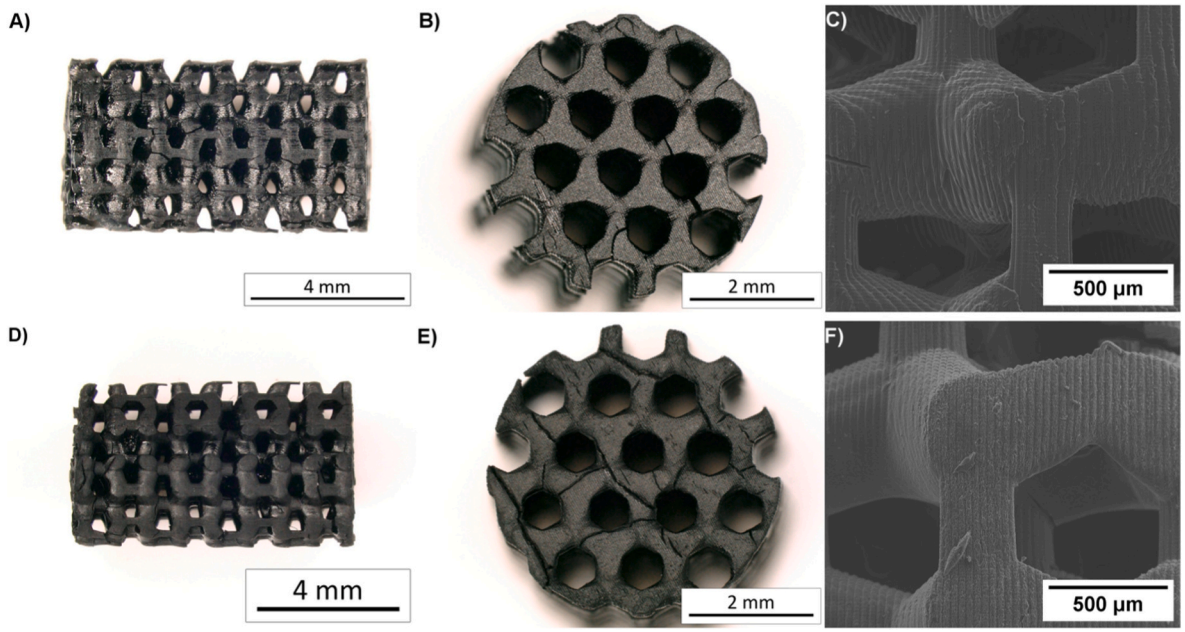

Fig. 6. Ceramic lattice structures of Ni-free reference and Ni-modified samples pyrolysed at 800 °C under Ar atmosphere at different magnifications, (A–C) Ni-free reference sample (Ref10T), (C–F) Ni-modified sample (5Ni10T).

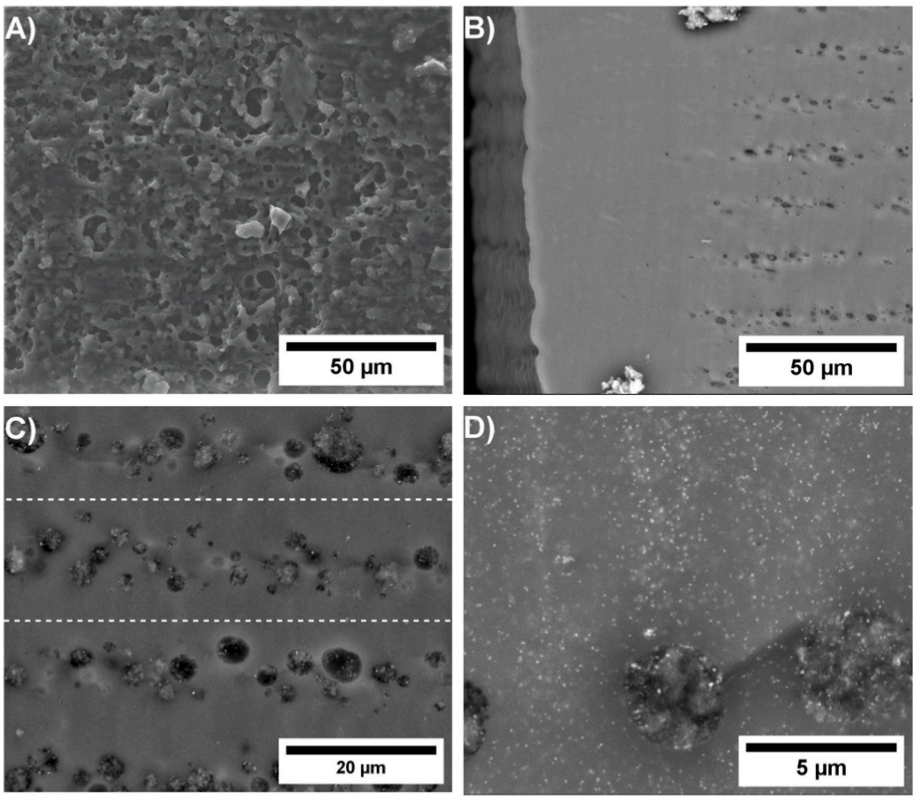

Fig. 7. SEM images of the Ni-modified ceramic material (5Ni10T) pyrolysed at 800 °C in Ar; A) Sample surface (secondary electron detector); B) Fracture surface at the edge of sample surface (backscatter electron detector); C) Fracture surface (backscatter electron detector; dashed lines indicating printing layer interface); D) Fracture surface (backscatter electron detector, higher magnification).

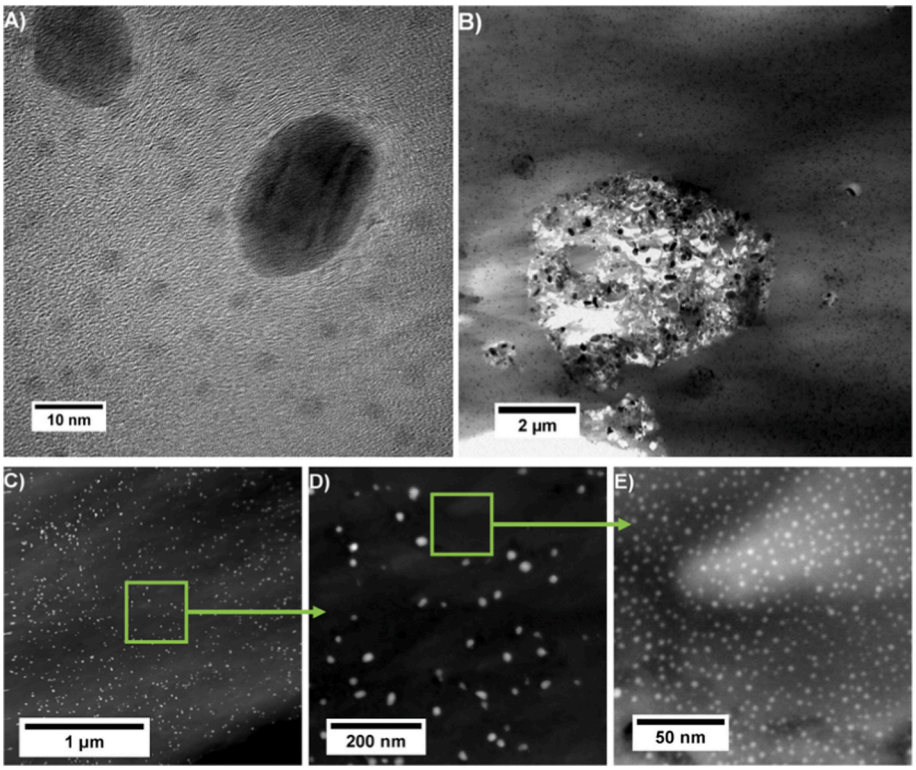

Fig. 8. TEM images of Ni particles within the SiOC matrix (sample 5Ni10T, after pyrolysis at 800 °C); A) HR-TEM image of bulk material with Ni particles of different sizes; B) TEM image of pore with Ni enrichments and surrounding bulk material; C-E) STEM HAADF images of bulk material with Ni particles, at several magnifications.

the sample. Below this dense outer layer, micelle-derived macropores appear within the material. The formation of a dense layer at the surface of photo-cured PDCs with a porous interior has been reported in the literature previously, being explained by the diffusion of non-cross-linked precursor components or carbon [42,43]. In comparison to the pore morphology in the printed state (Fig. 3C), which appears isotropic, after pyrolysis the pores appear located mainly in the center of the printing layers, suggesting a densification at the layer interface and retention of intra-layer porosity due to preferential diffusion through the interface [44].

Fig. 7C and D show higher magnifications of the interior of a Ni-modified material. In Fig. 7C, the compaction in the layer interface is again pointed out by marking the interface between the printing layers. Furthermore, a layer height of 15 μm can be observed after pyrolysis, which corresponds well with the intitial printing layer height by taking into account overall determined shrinkage of the specimens. As these images were recorded in backscattered electron mode, a contrast between the SiOC matrix and Ni particles is evident. Especially at higher magnification, Ni particles become visible both in the bulk material and within macropores. While indeed an accumulation of Ni in the pores appears to be present, the distribution in the material bulk appears homogeneous. The particles observable by SEM thus correspond to the first hierarchy of particles, at sizes between 10 and 30 nm.

To evaluate the size and morphology of the Ni particles within the SiOC matrix, TEM investigations were carried out. In Fig. 8 B, one of the pores derived from the micelles is shown, embedded in the Ni-modified SiOC matrix material. The dark Ni particles in the pores appear larger than those in the bulk material. The size difference may originate from incomplete solvation of nickel nitrate during resin preparation. In Fig. 8 A, a high-resolution TEM image depicts the Ni particles present in two size categories: in addition to the larger particles at a size of 10–30 nm, another hierarchy of particles sized in the range of 3 nm is evident. Especially at the interface between the large particles and the surrounding SiOC matrix, a layered structure can be seen. This structure may correlate with the formed nickel silicide ($NiSi_2$) phase found by XRD and SAED (Fig. 9A–B).

Although no uniform crystalline structure of particles was found in HR-TEM imaging, SAED signals could be assigned mainly to reflexes stemming from Ni and the $NiSi_2$ phase. This observation is also consistent with the XRD diffraction patterns recorded, confirming the Ni particles' crystallinity. STEM High Angle Annular Dark Field (HAADF) images were recorded to determine the particle size, providing a better contrast between particles and the SiOC matrix. Fig. 8 C-E provide a view of the particles in STEM HAADF mode which was used as a base for image-analysis-based particle size determination. Three different magnifications were selected to represent the different hierarchies of particle sizes. Again, a bimodal particle distribution was found, with particles at a size under 5 nm being present at a significantly higher number than particles with a size of 10–30 nm. According to image-analysis data, the larger crystalline particles have an average particle size of 16.1 nm ± 5.7 nm, while the smaller particle fraction shows an average particle size of 2.7 nm ± 0.7 nm. Nano-crystalline Ni particles have thus been successfully distributed homogeneously in the SiOC matrix.

As already discussed, the phase composition of the material was investigated by SAED and XRD, confirming the presence of both elemental Ni and $NiSi_2$ in crystalline form. Diffractograms were recorded after different heating temperatures to investigate the influence of the pyrolysis temperature on the phase development. In connection with the $NiSi_2$ phase development, no correlation with the pyrolysis temperature could be found. $NiSi_2$ is already present after pyrolysis at 600 °C, with no further accumulation at higher temperatures. Thus, a formation at temperatures below 600 °C can be anticipated. The formation of elemental Ni within metal-modified PDCs has been confirmed at temperatures below 400 °C, whereas the formation of $NiSi_2$ has so far only been described at temperatures above 850 °C in PSO systems [45,46]. The formation of $NiSi_2$ is generally associated with the presence of carbon in the system: in the case of the preceramic polymer system used in this work, a high free carbon content introduced through acrylates is causing the early formation of the silicide [12,15]. With regard to the catalytic activity of the material, the formation of $NiSi_2$ is not desirable, as this phase is generally considered to be catalytically inactive with regard to CO_2 methanation [47].

The results of physisorption data evaluated by the BET and BJH methods are shown in Table 3. After pyrolysis at 800 °C, both the Ni-free reference and the Ni-modified material exhibit a type II isotherm, indicating a macroporous material. An average pore size of 58.2 nm could be determined for the powdered, Ni-free reference material. While the printed reference samples exhibit a rather low specific surface area (SSA) of 0.12 m^2/g, the SSA is increased to 90.4 m^2/g as the sample is ground, suggesting a predominantly closed porosity within the bulk of the material due to the presence of a dense layer on the surface of the

Table 3
Specific surface area and average pore size (BJH-adsorption) of SiOC pyrolysed at 600 and 800 °C.

Sample	BET specific surface area ($m^2\ g^{-2}$)		Average pore size (nm)	
	component	powder	component	powder
Ref10T-600	132	366.8	2.2	2.8
Ref10T-800	0.12	90.4	–	58.2
5Ni10T-600	84.5	410.4	3.0	3.2
5Ni10T-800	1.6	19.9	6.2	6.4

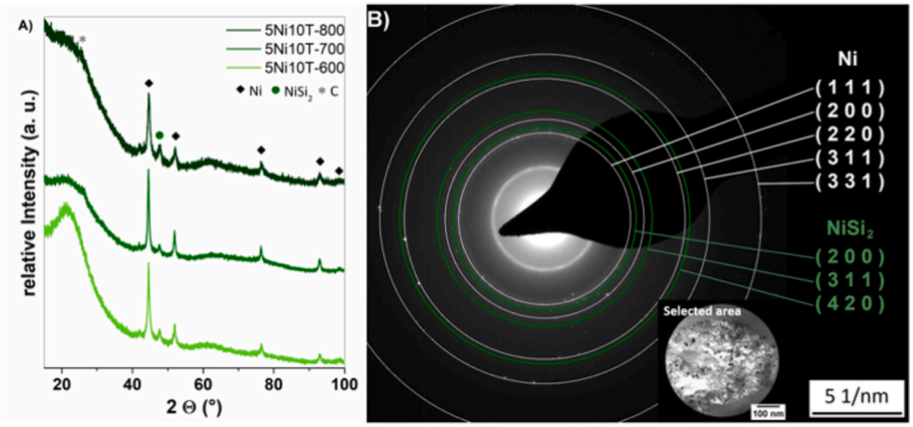

Fig. 9. A) X-ray diffractograms of Ni-modified ceramic (5Ni10T) after pyrolysis at 600, 700, and 800 °C; B) SAED image of Ni particles, with the indication of diffraction ring patterns characteristic for Ni and $NiSi_2$.

part (as mentioned in the previous section). The average pore size in the printed Ref10T-800 sample could not be determined using the BJH method because the total surface area was too low.

At a pyrolysis temperature of 600 °C, the SSA of the Ni-free SiOC materials increased up to 132 and 366 m^2/g in the component state and the powdered state, respectively. The adsorption-desorption isotherms of these samples correspond to a type IV isotherm indicating mesoporous materials, with average pore sizes of 2.2 and 2.8 nm for the components and the powdered materials, respectively. The increased surface area after pyrolysis at 600 °C can be attributed to presence of transient porosity during the polymer-to-ceramic conversion, which typically disappears at temperatures above 700 °C, the SSA thus decreasing as a result [48,49].

In terms of pore morphology and SSA, a comparable behavior can be observed for the Ni-containing materials. After pyrolytic conversion at 600 °C, even higher SSA values of 410 $m^2\ g^{-1}$ were determined for the powdered materials, while the components showed an SSA of 84.5 $m^2\ g^{-1}$, with average pore sizes in the range of 3 nm. Again, upon increasing the pyrolysis temperature, SSA values strongly decreased, while the average pore size increased to around 6 nm.

This difference in SSA between the component state and the powdered state strongly affects the catalysis performance, as discussed in chapter 3.5.

3.5. Catalytic properties

The catalytic performance of additively manufactured Ni-modified SiOC pyrolysed at different temperatures is summarized in Fig. 10. Catalytic measurements were performed with both actual printed components and ground specimens (sieved to <180 μm). Overall, printed components showed a comparably low catalytic activity, with CO_2 conversions between 0% and 3.5% for samples pyrolysed at 800 and 600 °C, respectively. In the sample pyrolysed at 600 °C, a selectivity to CH_4 of almost 10% can be achieved at 400 °C reaction temperature, while at 350 °C, only CO is produced. With ground samples, a CO_2 conversion of 25.6% can be reached at the maximum reaction temperature for the sample pyrolysed at 600 °C. For the same sample, the maximum value of selectivity to CH_4 is 53.4% at 400 °C.

Samples pyrolysed at 600 °C show higher catalytic activity than those pyrolysed at higher temperatures. On the one hand, this results from higher SSA values (Table 3). Furthermore, a difference in surface characteristics could be observed, influencing the catalytic activity: after pyrolysis at 600 °C, the materials exhibited a hydrophobic character, while at higher pyrolysis temperatures, the sample surface became hydrophilic. The absence of H_2O bands during ATR-FTIR investigations of samples pyrolysed at 600 °C is another indication for this hydrophobic behaviour (Fig. 4). As H_2O is a by-product during CO_2 methanation, hydrophobic surface properties can be considered beneficial toward the catalytic activity due to preventing water from blocking the adsorption

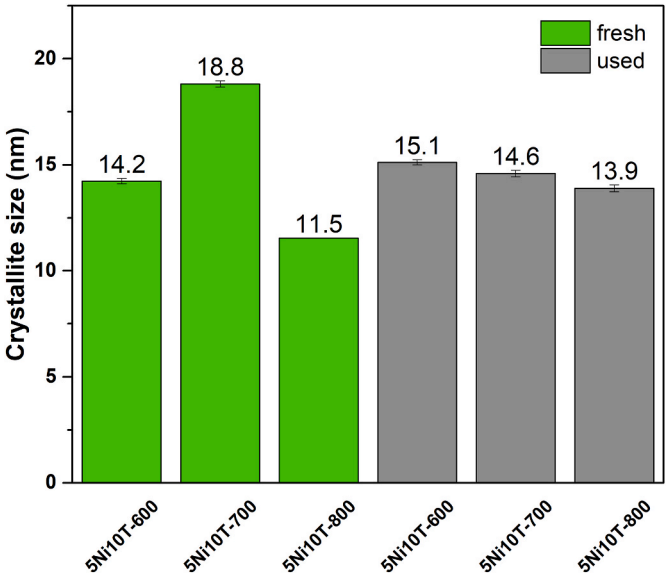

Fig. 11. Crystallite size of Ni-modified SiOC materials (5Ni10T) pyrolysed at distinct temperatures before and after catalysis experiments.

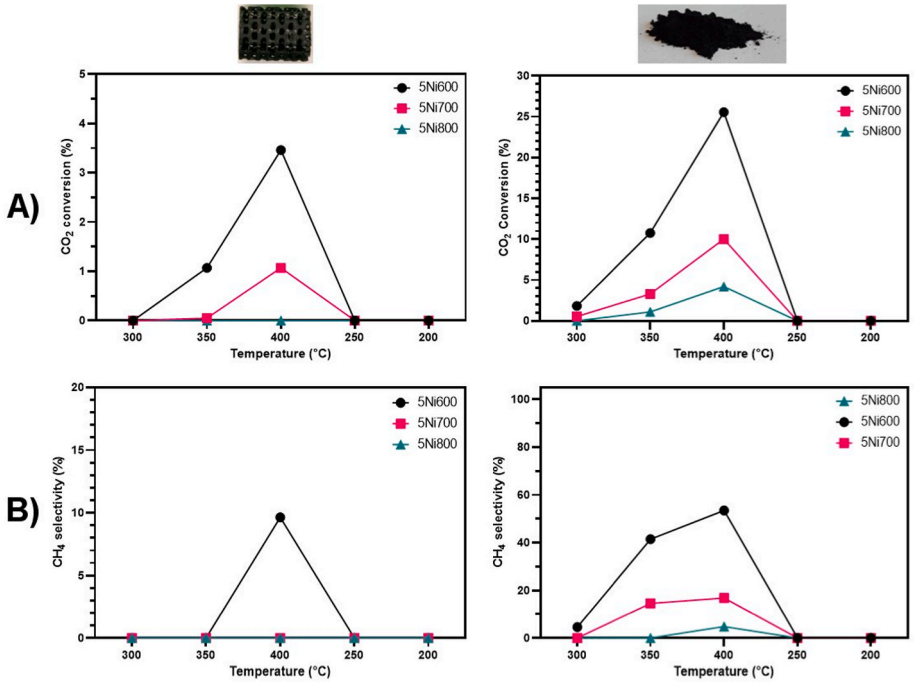

Fig. 10. (A) CO_2 conversion and (B) CH_4 selectivity of Ni-modified SiOC materials (5Ni10T) after pyrolysis at different temperatures (with catalysis testing temperatures shown in the order of testing): printed components (left) and ground samples (right).

sites [3]. The ground reference materials were tested to validate that the catalytic activity of the material indeed stems from the added Ni. Even though both reference materials (Ref10T-600 and Ref10T-800) showed minor catalytic activity during CO_2 conversion, no CH_4 formation could be detected.

Fig. 11 shows the crystallite sizes of Ni-modified PDCs pyrolysed at different temperatures before and after the catalytic reaction, determined from XRD data. In fresh samples, crystallite sizes between 11.5 and 18.8 nm were determined using the Scherrer Equation, which corresponds well with the size determination through TEM images of the bigger Ni particles in the SiOC matrix material (16.1 nm ± 5.7 nm). No significant effect of the pyrolysis temperature on the Ni particle size was found; the variations in crystallite size observed may indeed be attributed to method-specific inaccuracies. No crystallite growth was observed after the methanation reaction at temperatures up to 400 °C. The absence of crystallite growth can be seen as a distinct advantage over classically dispersed catalysts since a constant particle size generally accompanies a constant catalytic activity. The reason for the constant crystallite size can be seen in the strong bond between the particles and the PDC-based carrier matrix, as the separation of the particles leads to an absence of sintering phenomena [10].

4. Conclusions

In this work, a novel Ni-modified preceramic polymer system suitable for additive manufacturing by vat-based photopolymerization was developed. By investigating the processes during the photoreaction, it was possible to tailor the printing resin formulation toward the photopolymerization-based shaping process and thus achieve highly complex components with minimal printed strut sizes of 400 μm, demonstrating the generation of micrometric structures. Phase separation caused by nickel nitrate in the preceramic printing resin resulted in a stabilized emulsion, which resulted in a porous ceramic material structured by the emulsion micelles. The polymer-to-ceramic conversion was investigated by pyrolysis at 600–800 °C in Ar atmosphere. The introduction of Ni-based precursors resulted in the formation of nanometer-scaled Ni and $NiSi_2$ centers within the bulk ceramic matrix, with a bimodal size distribution and homogeneous spatial distribution. Process parameter-dependent effects on morphology, phase composition, and specific surface area in the ceramized materials were elucidated, and finally correlated to the materials' performance during catalytic testing. The Ni-modified, polymer-derived ceramic material exhibits a catalytic activity of the material with regard to CO_2 methanation, even though accessibility of the metal centers in printed components was limited compared to powdered materials due to the formation of dense surface layers. These initial catalytic results provide valuable information for future work on the generation of monolithic catalysts from polymer-derived metal-modified ceramics by vat-based photo-polymerization.

Declaration of competing interest

The authors declare that they have no known competing financial interests or personal relationships that could have appeared to influence the work reported in this paper.

Acknowledgements

Funding by the Austrian Research Promotion Agency (FFG) in the framework of the *PolyCAT3D* project (Grant. No. 877405) is gratefully acknowledged. This research was funded by the Austrian Science Fund (FWF, Schrödinger grant, J4460) and the European Research Council (ERC StG 640396 OPTIMALZ). The authors thank Prof. Robert Liska and Lisa Sinawehl for their support with photorheology investigations and Prof. Bernhard Lendl and Felix Frank for their help with FTIR measurements. Further appreciation goes to Detlef Burgard of RAHN AG for the provision of chemicals.

Appendix A. Supplementary data

Supplementary data to this article can be found online at https://doi.org/10.1016/j.oceram.2023.100350.

References

[1] P. Colombo, G. Mera, R. Riedel, G.D. Sorarù, Polymer-derived ceramics: 40 Years of research and innovation in advanced ceramics, J. Am. Ceram. Soc. 93 (7) (2010) 1805–1837.
[2] N. Yang, M. Gao, J. Li, K. Lu, Nickel-containing magnetoceramics from water vapor-assisted pyrolysis of polysiloxane and nickel 2,4-pentanedionate, J. Am. Ceram. Soc. 103 (1) (2020) 145–157.
[3] D. Schumacher, M. Wilhelm, K. Rezwan, Porous SiOC monoliths with catalytic activity by in situ formation of Ni nanoparticles in solution-based freeze casting, J. Am. Ceram. Soc. 103 (5) (2020) 2991–3001.
[4] S. Kaur, G. Mònego, K. Rezwan, M. Wilhelm, Synthesis of porous Ni/SiC(O)-Based nanocomposites: effect of nickel acetylacetonate and poly(ethylene glycol) methacrylate modification on specific surface area and porosity, Adv. Eng. Mater. (2019), 1901036.
[5] Y. Feng, Z. Yu, J. Schuch, S. Tao, L. Wiehl, C. Fasel, et al., Nowotny phase Mo 3+2 x Si 3 C 0.6 dispersed in a porous SiC/C matrix: a novel catalyst for hydrogen evolution reaction, J. Am. Ceram. Soc. 103 (1) (2020) 508–519.
[6] M. Zaheer, J. Hermannsdörfer, W.P. Kretschmer, G. Motz, R. Kempe, Robust heterogeneous nickel catalysts with tailored porosity for the selective hydrogenolysis of aryl ethers, ChemCatChem 6 (1) (2014) 91–95.
[7] V. Bakumov, K. Gueinzius, C. Hermann, M. Schwarz, E. Kroke, Polysilazane-derived antibacterial silver–ceramic nanocomposites, J. Eur. Ceram. Soc. 27 (10) (2007) 3287–3292.
[8] M. Zaheer, T. Schmalz, G. Motz, R. Kempe, Polymer derived non-oxide ceramics modified with late transition metals, Chem. Soc. Rev. 41 (15) (2012) 5102.
[9] J. Wang, V. Schölch, O. Görke, G. Schuck, X. Wang, G. Shao, et al., Metal-containing ceramic nanocomposites synthesized from metal acetates and polysilazane, Open Ceramics 1 (2020), 100001.
[10] H.P. Macedo, R.L.B.A. Medeiros, J. Ilsemann, D.M.A. Melo, K. Rezwan, M. Wilhelm, Nickel-containing hybrid ceramics derived from polysiloxanes with hierarchical porosity for CO2 methanation, Microporous Mesoporous Mater. 278 (2019) 156–166.
[11] N. Yang, K. Lu, Effects of transition metals on the evolution of polymer-derived SiOC ceramics, Carbon 171 (2021) 88–95.
[12] N. Yang, K. Lu, Phase content prediction in polymer-derived ceramics with metal additives, J. Am. Ceram. Soc. 104 (10) (2021) 5379–5391.
[13] E. Ionescu, C. Terzioglu, C. Linck, J. Kaspar, A. Navrotsky, R. Riedel, Thermodynamic control of phase composition and crystallization of metal-modified silicon oxycarbides, J. Am. Ceram. Soc. 96 (6) (2013) 1899–1903.
[14] S.M. Sachau, M. Zaheer, A. Lale, M. Friedrich, C.E. Denner, U.B. Demirci, et al., Micro-/Mesoporous platinum-SiCN nanocomposite catalysts (Pt@SiCN): from design to catalytic applications, Chem. Eur J. 22 (43) (2016) 15508–15512.
[15] M.G. Segatelli, A.T.N. Pires, I.V.P. Yoshida, Synthesis and structural characterization of carbon-rich SiCxOy derived from a Ni-containing hybrid polymer, J. Eur. Ceram. Soc. 28 (11) (2008) 2247–2257.
[16] E. Ionescu, B. Papendorf, H.-J. Kleebe, F. Poli, K. Müller, R. Riedel, Polymer-derived silicon oxycarbide/hafnia ceramic nanocomposites. Part I: phase and microstructure evolution during the ceramization process, J. Am. Ceram. Soc. 93 (6) (2010) 1774–1782.
[17] Y. Fu, G. Xu, Z. Chen, C. Liu, D. Wang, C. Lao, Multiple metals doped polymer-derived SiOC ceramics for 3D printing, Ceram. Int. 44 (10) (2018) 11030–11038.
[18] G. Glatz, T. Schmalz, T. Kraus, F. Haarmann, G. Motz, R. Kempe, Copper-containing SiCN precursor ceramics (Cu@SiCN) as selective hydrocarbon oxidation catalysts using air as an oxidant, Chem. Eur J. 16 (14) (2010) 4231–4238.
[19] T. Schmalz, T. Kraus, M. Günthner, C. Liebscher, U. Glatzel, R. Kempe, et al., Catalytic formation of carbon phases in metal modified, porous polymer derived SiCN ceramics, Carbon 49 (9) (2011) 3065–3072.
[20] M. Adam, M. Wilhelm, G. Grathwohl, Polysiloxane derived hybrid ceramics with nanodispersed Pt, Microporous Mesoporous Mater. 151 (2012) 195–200.
[21] M. Hojamberdiev, R.M. Prasad, C. Fasel, R. Riedel, E. Ionescu, Single-source-precursor synthesis of soft magnetic Fe3Si- and Fe5Si3-containing SiOC ceramic nanocomposites, J. Eur. Ceram. Soc. 33 (13–14) (2013) 2465–2472.
[22] S. Wang, J. Mao, Y. Liu, X. Lin, M. Sheng, C. Zhao, et al., Electromagnetic wave absorption properties of cobalt-containing polymer-derived SiCN ceramics, IOP Conf. Ser. Mater. Sci. Eng. 678 (2019), 012047.
[23] M. Balestrat, A. Lale, A.V.A. Bezerra, V. Proust, E.W. Awin, R.A.F. Machado, et al., In-situ synthesis and characterization of nanocomposites in the Si-Ti-N and Si-Ti-C systems, Molecules 25 (22) (2020) 5236.
[24] Q. Wen, Y. Xu, B. Xu, C. Fasel, O. Guillon, G. Buntkowsky, et al., Single-source-precursor synthesis of dense SiC/HfCxN1−x-based ultrahigh-temperature ceramic nanocomposites, Nanoscale 6 (22) (2014) 13678–13689.
[25] F. Bouzat, R. Lucas, Y. Leconte, S. Foucaud, Y. Champavier, C. Coelho Diogo, et al., formation of ZrC–SiC composites from the molecular scale through the synthesis of multielement polymers, Materials 14 (14) (2021) 3901.

[26] Z. Yu, K. Mao, Y. Feng, Single-source-precursor synthesis of porous W-containing SiC-based nanocomposites as hydrogen evolution reaction electrocatalysts, Journal of Advanced Ceramics 10 (2021) 1338–1349.
[27] A. Lale, M. Schmidt, M.D. Mallmann, A.V.A. Bezerra, E.D. Acosta, R.A.F. Machado, et al., Polymer-Derived Ceramics with engineered mesoporosity: from design to application in catalysis, Surf. Coating. Technol. 350 (2018) 569–586.
[28] J. Wang, M. Grünbacher, S. Penner, M.F. Bekheet, A. Gurlo, Porous silicon oxycarbonitride ceramics with palladium and Pd2Si nanoparticles for dry reforming of methane, Polymers 14 (17) (2022) 3470.
[29] Z. Yu, P. Zhang, Y. Feng, S. Li, Y. Pei, Template-free synthesis of porous Fe3O4/SiOC(H) nanocomposites with enhanced catalytic activity, J. Am. Ceram. Soc. 99 (8) (2016) 2615–2624.
[30] E. Zanchetta, M. Cattaldo, G. Franchin, M. Schwentenwein, J. Homa, G. Brusatin, et al., Stereolithography of SiOC ceramic microcomponents, Adv. Mater. 28 (2) (2016) 370–376.
[31] Z.C. Eckel, C. Zhou, J.H. Martin, A.J. Jacobsen, W.B. Carter, T.A. Schaedler, Additive manufacturing of polymer-derived ceramics, Science 351 (6268) (2016) 58–62.
[32] J. Essmeister, A.A. Altun, M. Staudacher, T. Lube, M. Schwentenwein, T. Konegger, Stereolithography-based additive manufacturing of polymer-derived SiOC/SiC ceramic composites, J. Eur. Ceram. Soc.42 13 (2022) 5343–5354.
[33] C. Ma, C. He, W. Wang, X. Yao, L. Yan, F. Hou, et al., Metal-doped polymer-derived SiOC composites with inorganic metal salt as the metal source by digital light processing 3D printing, Virtual Phys. Prototyp. (2020) 1–13.
[34] L. Yao, W. Yang, S. Zhou, H. Mei, L. Cheng, L. Zhang, Design paradigm for strong-lightweight perfect microwave absorbers: the case of 3D printed gyroid shellular SiOC-based metamaterials, Carbon 196 (2022) 961–971.
[35] S. Zhou, L. Yao, T. Zhao, H. Mei, L. Cheng, L. Zhang, Ti doped SiOC precursor to activate gyroid sensing structures, Carbon 196 (2022) 253–263.
[36] C. Gorsche, R. Harikrishna, S. Baudis, P. Knaack, B. Husar, J. Laeuger, et al., Real time-NIR/MIR-photorheology: a versatile tool for thein SituCharacterization of photopolymerization reactions, Anal. Chem. 89 (9) (2017) 4958–4968.
[37] A. Lichtenegger, D.J. Harper, M. Augustin, P. Eugui, M. Muck, J. Gesperger, et al., Spectroscopic imaging with spectral domain visible light optical coherence microscopy in Alzheimer's disease brain samples, Biomed. Opt Express 8 (9) (2017) 4007.
[38] W. Drexler, J.G. Fujimoto, Optical Coherence Tomography: Technology and Applications, Springer, 2015.
[39] C. Vakifahmetoglu, E. Pippel, J. Woltersdorf, P. Colombo, Growth of one-dimensional nanostructures in porous polymer-derived ceramics by catalyst-assisted pyrolysis. Part I: iron catalyst, J. Am. Ceram. Soc. 93 (4) (2010) 959–968.
[40] D. Wu, H. Zhang, Mechanical stability of monolithic catalysts: scattering of washcoat adhesion and failure mechanism of active, Material. Industrial & Engineering Chemistry Research 52 (41) (2013) 14713–14721.
[41] V. Palma, D. Barba, H2S purification from biogas by direct selective oxidation to sulfur on V2O5–CeO2 structured catalysts, Fuel 135 (2014) 99–104.
[42] J.J. Bowen, S. Mooraj, J.A. Goodman, S. Peng, D.P. Street, B. Roman-Manso, et al., Hierarchically porous ceramics via direct writing of preceramic polymer-triblock copolymer inks, Mater. Today 58 (2022) 71–79.
[43] Y. Fu, Z. Chen, G. Xu, Y. Wei, C. Lao, Preparation and stereolithography 3D printing of ultralight and ultrastrong ZrOC porous ceramics, J. Alloys Compd. 789 (2019) 867–873.
[44] S. Xiong, J. Liu, J. Cao, Z. Li, M. Idrees, X. Lin, et al., 3D printing of crack-free dense polymer-derived ceramic monoliths and lattice skeletons with improved thickness and mechanical performance, Addit. Manuf. 57 (2022), 102964.
[45] M. Scheffler, P. Greil, A. Berger, E. Pippel, J. Woltersdorf, Nickel-catalyzed in situ formation of carbon nanotubes and turbostratic carbon in polymer-derived ceramics, Mater. Chem. Phys. 84 (1) (2004) 131–139.
[46] N. Asakuma, S. Tada, E. Kawaguchi, M. Terashima, S. Honda, R.K. Nishihora, et al., Mechanistic investigation of the Formation of nickel nanocrystallites embedded in amorphous silicon nitride nanocomposites, Nanomaterials 12 (10) (2022) 1644.
[47] C. Hoffmann, P. Plate, A. Steinbrück, S. Kaskel, Nanoporous silicon carbide as nickel support for the carbon dioxide reforming of methane, Catal. Sci. Technol. 5 (8) (2015) 4174–4183.
[48] T. Konegger, C. Drechsel, H. Peterlik, In-situ small angle X-ray scattering (SAXS) – a versatile tool for clarifying the evolution of microporosity in polymer-derived ceramics, Microporous Mesoporous Mater. 324 (2021), 111268.
[49] T. Konegger, C.-C. Tsai, H. Peterlik, S.E. Creager, R.K. Bordia, Asymmetric Polysilazane-Derived Ceramic Structures with Multiscalar Porosity for Membrane Applications, vol. 232, 2016, pp. 196–204.